

# First-principles Investigation of Thermodynamic Properties of $\text{CrNbO}_4$ and $\text{CrTaO}_4$

**Shuang Lin**<sup>1</sup>, Shun-Li Shang<sup>1</sup>, Allison M. Beese<sup>1,2</sup>, and Zi-Kui Liu<sup>1</sup>

<sup>1</sup> Department of Materials Science and Engineering, The Pennsylvania State University,  
University Park, PA, 16802, USA

<sup>2</sup> Department of Mechanical Engineering, The Pennsylvania State University,  
University Park, PA 16802, USA

## 1 Abstract

In the present study, the DFT+U method was employed to predict the thermodynamic properties of  $\text{Cr}_2\text{O}_3$ ,  $\text{Nb}_2\text{O}_5$ , and  $\text{Ta}_2\text{O}_5$ . Results were benchmarked with experimental data showing high accuracy, except for the negative thermal expansion (NTE) of  $\text{Nb}_2\text{O}_5$ , which is attributed to its polymorphic complexity. Additionally, we extended our analysis to rutile-type oxides  $\text{CrNbO}_4$  and  $\text{CrTaO}_4$ , examining their entropy and heat capacity at finite temperatures.  $\text{CrNbO}_4$  displayed slightly higher entropy and heat capacity at high temperatures. The mean linear thermal expansion coefficients for  $\text{CrNbO}_4$  and  $\text{CrTaO}_4$  from 500 K to 2000 K were predicted to be  $6.00 \times 10^{-6}/\text{K}$  and  $13.49 \times 10^{-6}/\text{K}$ , respectively, corroborating with DFT predictions and experimental evidence. Our research highlights the precision of the DFT+U and phonon methods in predicting the thermodynamic properties of oxide materials, offering insights into the design of corrosion-resistant materials.

## 1. Introduction

Refractory High Entropy Alloys (RHEAs) are increasingly recognized as innovative and promising materials for ultrahigh high-temperature environments, primarily due to their superior mechanical properties [1]. However, significant concerns have been raised regarding the oxidation behavior of RHEAs at elevated temperatures. For example,  $V_2O_5$  melts at temperatures above  $675^\circ\text{C}$ , while  $MoO_3$  and  $WO_3$  are prone to evaporation at temperatures exceeding  $795^\circ\text{C}$  and  $1000^\circ\text{C}$ , respectively [2]. The most critical challenge with RHEAs is their tendency not to form coherent, self-protective surface oxide scales like  $Al_2O_3$ ,  $Y_2O_3$ , or  $SiO_2$ . This limitation is attributed to the very low solubility of refractory metals in elements like Al, Y, or Si. Additionally, adding elements like Si to form Si-containing RHEAs can lead to increased internal corrosion attack. While  $Cr_2O_3$  has been recognized as a protective oxide in steels and nickel-based superalloys, its use in refractory metals for ultra-high temperature applications is also limited since its volatility is influenced by water vapor pressure at temperatures beyond  $950^\circ\text{C}$  [3–5].

Recent studies have highlighted the effectiveness of two rutile-type oxides,  $CrNbO_4$  and  $CrTaO_4$ , in enhancing the oxidation resistance of various alloys. Specifically, investigations have demonstrated improved thermal cycling oxidation resistance in Nb-Cr-Si-based alloys. This improvement is linked to the formation of coherent  $CrNbO_4$  layers instead of  $Nb_2O_5$  [3,6,7]. Additionally, the presence of  $CrNbO_4$  at the interface between metal and oxide in Nb-Si based alloys contributes to a stronger adherence between the oxide scale and the substrate [8]. In the case of equimolar TaMoCrTiAl RHEAs at  $1000^\circ\text{C}$ , the alloy's exceptional oxidation resistance in an air environment is attributed to the formation of protective  $CrTaO_4$  oxide layers. These layers play a crucial role in significantly impeding oxygen diffusion, thereby enhancing the alloy's

performance under high-temperature conditions [9]. However, there is limited information on the thermodynamic properties of these two rutile type oxides, and the present study aims to provide them using first-principles calculations based on density functional theory (DFT). Having these thermodynamic properties available is critically important to further aid the design of refractory high entropy alloys with enhanced oxidation resistance.

## 2. First-principles calculations

### 2.1 First-principles quasiharmonic approach

DFT-based first-principles calculations are inherently predictive as they rely solely on the atomic species and crystal structure information. These methods provide insights into quantities linked to the electronic structure and the Helmholtz free energy ( $F$ ) of a specific structure as a function of volume ( $V$ ) and temperature ( $T$ ). Within the framework of the quasiharmonic approach,  $F$  is represented by [10–12],

$$F(V, T) = E_c(V) + F_{vib}(V, T) + F_{ele}(V, T) \quad \text{Eq. 1}$$

where  $E_c$  represents the static energy at 0 K as predicted by first-principles calculations,  $F_{vib}$  is the vibrational component of the free energy, and  $F_{ele}$  denotes the thermal electronic contribution to free energy. This latter component is derived through integration over the electronic density of states (DOS), in accordance with the Fermi-Dirac distribution [10–12]. We adopt the four-parameter Birch–Murnaghan equation of state (EOS) to estimate  $E_c$  based on first-principles calculated E-V (energy-volume) data points. The linear form of this equation is described by [11],

$$E_c(V) = a + bV^{-2/3} + cV^{-4/3} + dV^{-2} \quad \text{Eq. 2}$$

where  $a$ ,  $b$ ,  $c$ , and  $d$  are fitting parameters. The equilibrium properties estimated from EOS include volume ( $V_0$ ), energy ( $E_0$ ), bulk modulus ( $B_0$ ) and its pressure derivative ( $B'_0$ ).

The vibrational free energy is obtained by phonon calculations in the present work. Based on the distribution of phonon frequency  $\omega$  at given volume, the vibration contribution to the Helmholtz free energy can be written as follows according to the partition function of lattice vibration [10–12],

$$F_{vib}(V, T) = k_B T \int_0^{\infty} \ln \left[ 2 \sinh \frac{\hbar \omega}{2 k_B T} \right] g(\omega) d(\omega) \quad \text{Eq. 3}$$

where  $k_B$  is the Boltzmann constant,  $\hbar$  is the reduced Planck constant, and  $g(\omega)$  is the phonon DOS.

## 2.2 Details of first-principles and phonon calculations

All DFT-based first-principles calculations in the present work were performed by the Vienna Ab initio Simulation Package (VASP) [13] using the projector augmented wave (PAW) method [14]. The exchange-correlation functional was described by the generalized gradient approximation (GGA) of Perdew, Burke, and Ernzerhof [15]. Different  $k$ -point meshes (details in Table 1) together with a 350 eV plane wave cutoff energy were employed based on our convergence tests. The energy convergence criterion of electronic self-consistency was chosen as  $1 \times 10^{-6}$  eV per supercell in all the calculations. The reciprocal space energy integration was performed by the Methfessel-Paxton technique [16] for structural relaxations with a 0.2 eV smearing width. For static calculations at 0 K, we adopted the PAW method and the rotationally invariant DFT+U approach of Liechtenstein [17], as implemented in VASP. The outcome of these calculations is contingent upon the effective on-site Coulomb (U) and exchange (J) parameters, which were set to U=4.5 eV and J=1.0 eV for the d orbitals of Cr [ref]. The initial magnetic moment of Cr is set

as 5  $\mu\text{B}$ . For phonon calculations, we employ the supercell method [18], using YPHON [19] package, with VASP again as the computational engine. Details of supercell size, k-point mesh, and the final cutoff distance to fit force constants and to calculate phonon properties for each oxide are given in Table 1.

Table 2 presents the lattice parameters of  $\text{Cr}_2\text{O}_3$ ,  $\text{Nb}_2\text{O}_5$ ,  $\text{Ta}_2\text{O}_5$ ,  $\text{CrNbO}_4$ , and  $\text{CrTaO}_4$  from the present work. For the binary oxides, the most stable structures were selected, which are deemed the precursors for forming  $\text{CrNbO}_4$  and  $\text{CrTaO}_4$ . The primitive unit cell of  $\text{Cr}_2\text{O}_3$  exhibits a rhombohedral geometry with lattice parameters being 5.3412 Å and  $55.10^\circ$ , which are within 0.2% of the experimental values of 5.35 Å and  $55.15^\circ$  [20]. Our calculations confirm that the antiferromagnetic configuration with four Cr atoms in the primitive unit cell results in the minimal energy state. The structures of  $\text{Nb}_2\text{O}_5$  and  $\text{Ta}_2\text{O}_5$  were chosen based on the lowest formation energies reported in the Materials Project database (mp-1595 and mp-1392387) [21], the energy above the formation energy convex hull for these structures are within 0.01 eV/atom. The structures of  $\text{CrNbO}_4$  and  $\text{CrTaO}_4$  are based on the prototype of the rutile phase in  $\text{TiO}_2$ , where Cr and Nb (or Ta) are octahedrally coordinated, each surrounded by six oxygen atoms, as also reported by experimental synthesis [22].

### **3. Results and discussion**

#### **3.1 Ground state configuration of the $\text{CrNbO}_4$ and $\text{CrTaO}_4$**

Due to the magnetic nature of Cr, we examined the relaxed energies of  $\text{CrNbO}_4$  and  $\text{CrTaO}_4$  using four independent spin-polarized configurations as determined by symmetry analysis with the Alloy

Theoretic Automated Toolkit (ATAT) [23]. The magnetic configurations for Cr are detailed in Table 3, with Cr1 through Cr4 corresponding to the positions of Cr as depicted in Figure 1 and Figure 2. The "↑" symbol denotes an upwards Cr spin, while "↓" represents a downwards Cr spin. Our findings indicate that the spin of Cr does not substantially change the energy of CrNbO<sub>4</sub>, evidenced by the negligible energy differences among the four configurations, which are within 0.001 eV per supercell. The configuration with the lowest energy is designated as str1, displaying a ferromagnetic arrangement. In CrTaO<sub>4</sub>, significant energy difference is observed between the energies of str1, str2, and str4, with str3 exhibiting an energy comparable to that of str1. In the literature, the magnetic measurement indicates there is the competition between the antiferromagnetic and ferromagnetic interactions at low temperature [22]. In our current study, we employ the exchange interactions approach (DFT+U) to strongly correlated d or f electrons, which can contribute to the increased energy states of both CrNbO<sub>4</sub> and CrTaO<sub>4</sub>. Consequently, the ferromagnetic spin configuration for both compounds is considered as the ground state and has been adopted for subsequent first-principles calculations.

### 3.2 Thermodynamic properties of binary oxides, Cr<sub>2</sub>O<sub>3</sub>, Nb<sub>2</sub>O<sub>5</sub> and Ta<sub>2</sub>O<sub>5</sub>

In the present study the entropy, heat capacity, and linear thermal expansion of Cr<sub>2</sub>O<sub>3</sub>, Nb<sub>2</sub>O<sub>5</sub>, and Ta<sub>2</sub>O were calculated using phonon approach, and compared with experimental data and values from the SSUB5 database in Thermo-Calc 2016 [24,25]. Figure 3 presents the entropies of these three binary oxides. The entropy of Cr<sub>2</sub>O<sub>3</sub> in the present study is 2-10 J/mol·K lower than that in the SSUB5 database. At higher temperature, the difference becomes larger. [26] In Figure 4, the heat capacity (C<sub>p</sub>) of Cr<sub>2</sub>O<sub>3</sub> exhibits a lambda-shaped at the Néel temperature 307K, indicative of antiferromagnetic ordering, as measured by Anderson [27] and Gurevich [28]. The present study

does not take into account the Néel transition at 307 K, leads to an underestimation of entropy and a poor agreement of heat capacity ( $C_p$ ) around 300 K, which could be studied in terms of the entropy theory [29–32] though out of the scope of the present study. Our  $C_p$  predictions are lower compared to those derived from SSUB5. This discrepancy can be attributed to the fact that SSUB5, when establishing the  $\text{Cr}_2\text{O}_3$  database, relied on the high-temperature  $C_p$  data from Moore and Kelly [33]. Additionally, our results show only minimal differences when compared to phonon calculations using the LDA+U approach [34], which is in very good agreement with the high-temperature measurements of Ziemiak [35]. It is important to note that the heat capacity data measured by Ziemiak through calorimetry had a standard deviation of  $\pm 3\%$  at temperature below 1673 K and  $\pm 5\%$  between 1673 and 1873 K. This variability underlines the precision of the phonon calculations in our work, especially in accurately predicting  $C_p$  at temperatures above 700 K.

Thermal expansion is a critical thermodynamic parameter for  $\text{Cr}_2\text{O}_3$ , especially for its application as a high-temperature coating material. Figure 5 plots the calculated linear thermal expansion coefficient of  $\text{Cr}_2\text{O}_3$  with empirical data from Huntz et al. [36] and Zhao et al. [37] superimposed. Our work predicts a higher expansion coefficient than Wang's findings [34] upto 1500 K, with the largest being  $0.5 \times 10^{-6}/\text{K}$ . This variance can be explained by the LDA potential underestimating lattice parameters, resulting in stiffer interatomic force constants, while PBE potential overestimates these parameters, leading to softer constants [38]. Furthermore, the measurements of linear thermal expansion coefficients of  $\text{Cr}_2\text{O}_3$  are quite scattered, ranging from  $5.7 \times 10^{-6}/\text{K}$  to  $10.75 \times 10^{-6}/\text{K}$  [34,36,37,39].



The predicted entropy for  $\text{Nb}_2\text{O}_5$  agrees well with the SSUB5 database and with Jacob's reassessment [36] across the temperature range of 298.15 K to 1700 K. The recalculated activity of niobium in stoichiometric  $\text{Nb}_2\text{O}_5$  is found to be  $6.097 \times 10^{-30}$ . Upon reevaluation, both the activity of niobium and the Gibbs energy of mixing for the  $\text{Nb}_2\text{O}_{5-x}$  phase have been updated. This revision leads to a more accurate match of the phase boundary data. Furthermore, it's noteworthy that the Gibbs formation energy for this phase is now determined to be more positive by 1.23 kJ/mol when compared to the values reported in the JANAF thermochemical tables [37]. Beyond 1800 K, the SSUB5 entropy values exceed our calculations, attributable to surpassing the melting point of  $\text{Nb}_2\text{O}_5$  at approximately 1780 K. Our predictions are confined to the solid phase of  $\text{Nb}_2\text{O}_5$ , which explains the divergence when  $\text{Nb}_2\text{O}_5$  transitions to the liquid phase. The predicted heat capacity of  $\text{Nb}_2\text{O}_5$  agrees well with SSUB5 and Jacob's reassessment [36] up to 800 K, with a slight underestimation observed thereafter, up to 2.0 J/mol·K. This can be explained by the greater contribution of anharmonic effects at elevated temperatures, which significantly cause the deviations heat capacity from quasiharmonic behavior [38]. The literature report that for  $\text{Fe}_3\text{Pt}$ , quasiharmonic approximation is quite effective in predicting the entropy for each configuration at lower temperatures from 0 K to 600K. However, at higher temperatures, the emergence of Negative Thermal Expansion (NTE) behavior is attributed to a significant increase in the number of symmetry-breaking, non-ground-state configurations. These configurations have smaller volumes compared to the ground-state configuration. It's important to note that none of these individual configurations exhibit NTE on their own. This indicates that the anharmonic effects become more pronounced at elevated temperatures, leading to a more complex thermal behavior that deviates from the predictions of the quasiharmonic approximation [38]. The SSUB5 database

indicates a discontinuity at 1780 K, corresponding to the phase transition due to the melting of Nb<sub>2</sub>O<sub>5</sub>.

The phonon model predicts a NTE for Nb<sub>2</sub>O<sub>5</sub> from 0 to 250 K, which is supported by literature evidencing NTE at low temperatures, although results quite dispersed from different literatures. Manning's [39] showed that the coefficients of thermal expansion (CTE) for monoclinic H-Nb<sub>2</sub>O<sub>5</sub> along the a, b, and c axes are  $5.3 \times 10^{-6}/\text{K}$ , 0, and  $5.9 \times 10^{-6}/\text{K}$ , respectively, from room temperature to 1350°C, revealing that its lattice thermal expansion is anisotropic. Manning's research also investigates the examination of hot-pressed samples during heating and cooling cycles ranging from 273 K to 1473 K. The paper details the percentage change in dimensions corresponding to varying temperatures. To align this with our predictions, we calculated the analytical slope of the temperature percentage, yielding the CTE in comparable units, as depicted in Figure 5. Durbin [40] also reported the low thermal expansion in sintered polycrystalline Nb<sub>2</sub>O<sub>5</sub>, as measured using a dilatometer with data obtained during heating only. They discovered that the mean CTE was  $0.483 \times 10^{-6}/\text{K}$  from 25 to 900°C, but also show the negative CTE under the low temperature. The analytical CTE is also plotted in Figure 5, where we utilize the percentage change data from the Durbin's study.

Douglass [41] employed a dilatometer to measure the linear thermal expansion of both stoichiometric and nonstoichiometric hot-pressed Nb<sub>2</sub>O<sub>5</sub>. The variations in CTE between these two forms were minor, with the nonstoichiometric oxides exhibiting slightly higher values. From Douglass's data, the average expansion coefficient from 20 to 900°C was calculated to be  $1.593 \times 10^{-6}/\text{K}$ , a value approximately three times higher than that reported by Durbin. The primary reason for this discrepancy in CTE values appears to be linked to the differences in sample fabrication techniques used by Manning, Durbin and Douglass [39–41]. It is suggested that the

hot-pressed samples, being devoid of internal microcracks, exhibit different thermal expansion properties. This is supported by the observed  $2.19 \times 10^{-6}/\text{K}$  overall expansion coefficient from room temperature to  $1000^\circ\text{C}$  for hot-pressed samples, compared to  $1.66 \times 10^{-6}/\text{K}$  for a sintered sample with the same porosity [39]. The hot-pressing process, conducted at high temperatures, is able to influence the material's thermal response, leading to the observed variations in CTE.

In Choosuwan's investigation [42], using dilatometry, both ceramic and single crystal  $\text{Nb}_2\text{O}_5$  specimens were studied for thermal expansion across a temperature range of 20 to  $500^\circ\text{C}$ , with a focus on cyclic heating and cooling. The findings showed a distinct region of negative CTE in these materials, the average coefficient was measured at  $-2 \times 10^{-6}/\text{K}$  before reaching  $200^\circ\text{C}$ , and it further decreased to  $-4 \times 10^{-6}/\text{K}$  after  $300^\circ\text{C}$ . Remarkably, all specimens exhibited negative linear expansion in directions both parallel and perpendicular to their growth axis. This unique phenomenon can be further understood through Choosuwan's investigation into the CTE of single-crystal  $\text{Nb}_2\text{O}_5$ . In single crystals, the atomic arrangement and bonding forces are highly uniform and directional. Such uniformity in the crystal structure can lead to anisotropic thermal behavior, where the material exhibits different thermal expansion properties in different directions. In the case of  $\text{Nb}_2\text{O}_5$ , these unique structural characteristics result in a contraction upon heating, leading to a negative CTE. This effect is more significant in single crystals due to their highly ordered and consistent atomic structure, as compared to polycrystalline materials where the crystal orientations are more random and varied.

The significant variation in the CTE of  $\text{Nb}_2\text{O}_5$  can be also attributed to its complex polymorphism, with over 15 reported structures [43,44]. Brauer's [45] research identified three primary crystalline forms of  $\text{Nb}_2\text{O}_5$ , each transforming under heat: amorphous to  $\gamma$ -phase at  $500^\circ\text{C}$ ,  $\gamma$  to  $\beta$ -phase at  $1000^\circ\text{C}$ , and  $\beta$  to  $\alpha$ -phase at  $1100^\circ\text{C}$ . Schaefer et al. [46] further noted that all  $\text{Nb}_2\text{O}_5$  forms

eventually and rapidly convert to the monoclinic Nb<sub>2</sub>O<sub>5</sub> at temperatures exceeding 1100°C, which is recognized as the high-temperature stable phase. This irreversible transformation to the monoclinic structure supports the understanding of its stability and likely contributes to the observed variability in Nb<sub>2</sub>O<sub>5</sub>'s thermal expansion properties.

The predicted entropy for Ta<sub>2</sub>O<sub>5</sub> aligns closely with the SSUB5 database and Jacob's findings [51] until 1593K, beyond which phonon predictions give a lower entropy. This discrepancy is attributed to the phase transition from  $\beta$  to  $\alpha$  at 1593K, a factor not accounted for in the present work. Similarly, the heat capacity of Ta<sub>2</sub>O<sub>5</sub> is in agreement with the measurements made by Orr [52] up to  $T = 1593$  K. Regarding thermal expansion, Yoon [53] reported a mean coefficient of thermal expansion (CTE) for Ta<sub>2</sub>O<sub>5</sub> thin films produced via single and dual ion beam sputtering methods as  $4.68 \times 10^{-6}/\text{K}$  from 50°C to 200°C. Wu [54] found that undoped Ta<sub>2</sub>O<sub>5</sub> had a CTE of  $6.72 \times 10^{-6}/\text{K}$  from room temperature to 1000°C. Additionally, Tien's [55] research indicated that between 25 to 55°C, the CTE of Ta<sub>2</sub>O<sub>5</sub> films is  $3.6 \times 10^{-6}/\text{K}$ . The predicted CTE values for Ta<sub>2</sub>O<sub>5</sub> closely align with these experimental results, displaying a minor deviation of approximately  $1 \times 10^{-6}/\text{K}$ . This consistency underscores the high accuracy of the phonon method in predicting the thermal properties of Ta<sub>2</sub>O<sub>5</sub>.

### 3.3 Thermodynamic properties of CrNbO<sub>4</sub> and CrTaO<sub>4</sub>

Employing the same phonon methodology used for binary oxides, the thermodynamic properties of CrNbO<sub>4</sub> and CrTaO<sub>4</sub> are predicted. This involved examining phonon dispersions within the quasi-harmonic approximation across five different volumes to accurately determine the entropy,

heat capacity, and coefficients of thermal expansion at finite temperature. As shown in Figure 6, at lower temperatures, the entropy of CrNbO<sub>4</sub> and CrTaO<sub>4</sub> exhibits close similarity. However, with rising temperatures, a divergence becomes evident; at 1000K, the entropy of CrNbO<sub>4</sub> surpasses that of CrTaO<sub>4</sub> by around 1 J/mol·K. Figure 6 also presents the Cp for both oxides, showing similarity at temperatures below 250 K and a difference of up to 1.5 J/mol·K compared to CrTaO<sub>4</sub> at high temperature.

The CTEs for the two oxides, CrNbO<sub>4</sub> and CrTaO<sub>4</sub>, are significant different from each other. To facilitate comparison with experimental findings, we converted the volumetric CTE values into linear thermal expansion coefficients by dividing them by 3. From 500K to 2000 K, the mean linear thermal expansions of CrNbO<sub>4</sub> and CrTaO<sub>4</sub> are approximately  $6.00 \times 10^{-6}/\text{K}$  and  $13.49 \times 10^{-6}/\text{K}$ , respectively. Tabero's [56] used high-temperature X-ray diffractometry and reported the thermal expansion of CrNbO<sub>4</sub> as  $5 \times 10^{-6}/\text{K}$ ,  $5 \times 10^{-6}/\text{K}$ , and  $8 \times 10^{-6}/\text{K}$  along the a, b, and c axes, respectively. The corresponding volumetric CTE is  $17.8 \times 10^{-6}/\text{K}$  in the range from 298K to 1073K. Figure 6 includes the Hao's predictions for CrTaO<sub>4</sub> [5] using a similar phonon approach for the rutile-type structure with overall agreement with our predictions. The observed differences could stem from variations in the settings for cutoff energy and k-point meshes. These data for both oxides are important in designing corrosion-resistant alloys with similar CTEs.

#### **4. Conclusions**

In the present study, the DFT+U approach is employed to predict the thermodynamic properties of Cr<sub>2</sub>O<sub>3</sub>, Nb<sub>2</sub>O<sub>5</sub>, and Ta<sub>2</sub>O<sub>5</sub>, including entropy, heat capacity, and linear thermal expansion

coefficient as a function of temperature in comparison with experimental data in the literature. Our predictions closely matched experimental findings for all assessed thermodynamic properties, except the NTE for  $\text{Nb}_2\text{O}_5$ , which may be predicted by the zentropy theory. The benchmarked approach is then used to investigate the thermodynamic properties of two rutile-type oxides,  $\text{CrNbO}_4$  and  $\text{CrTaO}_4$ . It is predicted that from 500K to 2000K, the mean linear CTEs of  $\text{CrNbO}_4$  and  $\text{CrTaO}_4$  were approximately  $6.00 \times 10^{-6}/\text{K}$  and  $13.49 \times 10^{-6}/\text{K}$ , respectively, in agreement with available experimental data. Our findings underscore the effectiveness of DFT+U and phonon methods in accurately predicting the thermodynamic behavior of complex oxide materials, paving the way for future advancements in corrosion-resistant materials design.

## **5. Acknowledgements**

The present work is based upon work supported by the Department of Energy/Advanced Research Projects Agency - Energy (ARPA-E) under award No DE-AR0001435. First-principles calculations were performed partially on the Roar Collab supercomputer at the Pennsylvania State University's Institute for Computational and Data Sciences (ICDS), and partially on the resources of the Extreme Science and Engineering Discovery Environment (XSEDE) supported by NSF with Grant No. ACI-1548562.

## 6. Figures

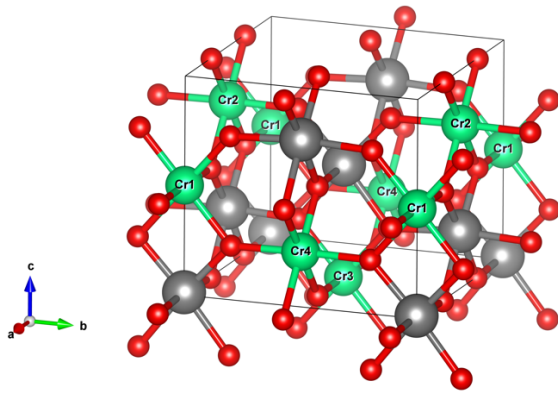


*Figure 1. Crystal structure of CrNbO<sub>4</sub>*



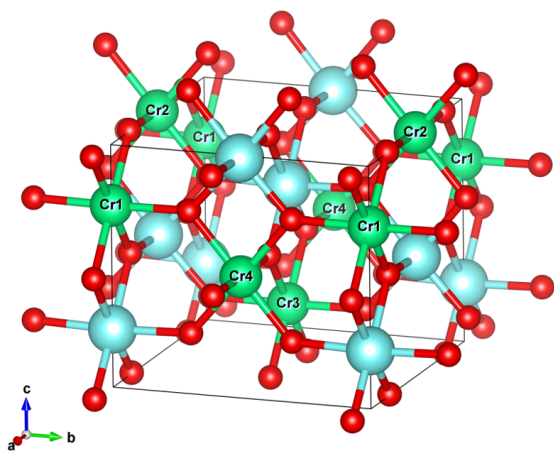


Figure 2. Crystal structure of CrTaO<sub>4</sub>

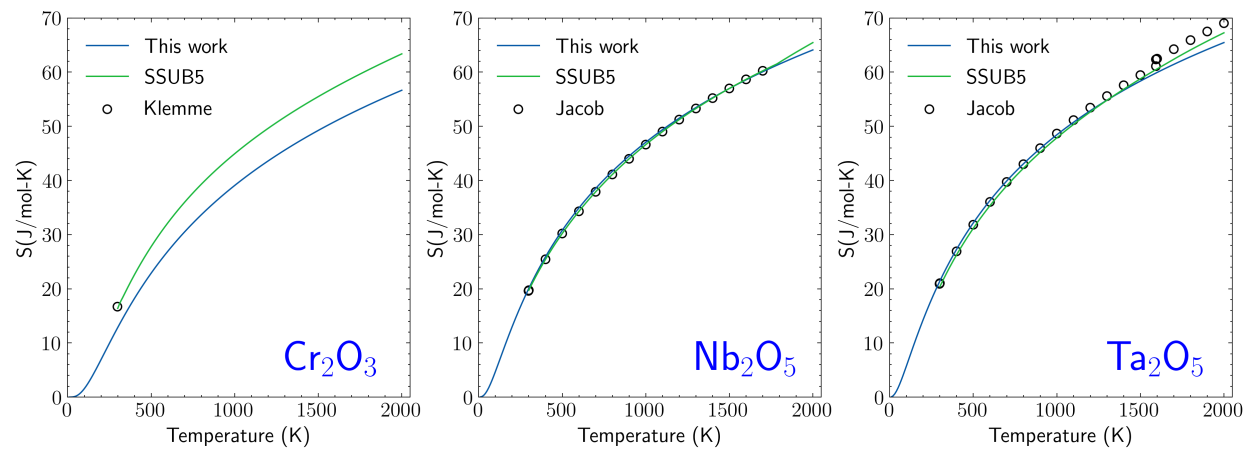


Figure 3. Entropy prediction of  $\text{Cr}_2\text{O}_3$ ,  $\text{Nb}_2\text{O}_5$  and  $\text{Ta}_2\text{O}_5$ , comparison with SSUB5 database and experimental data.

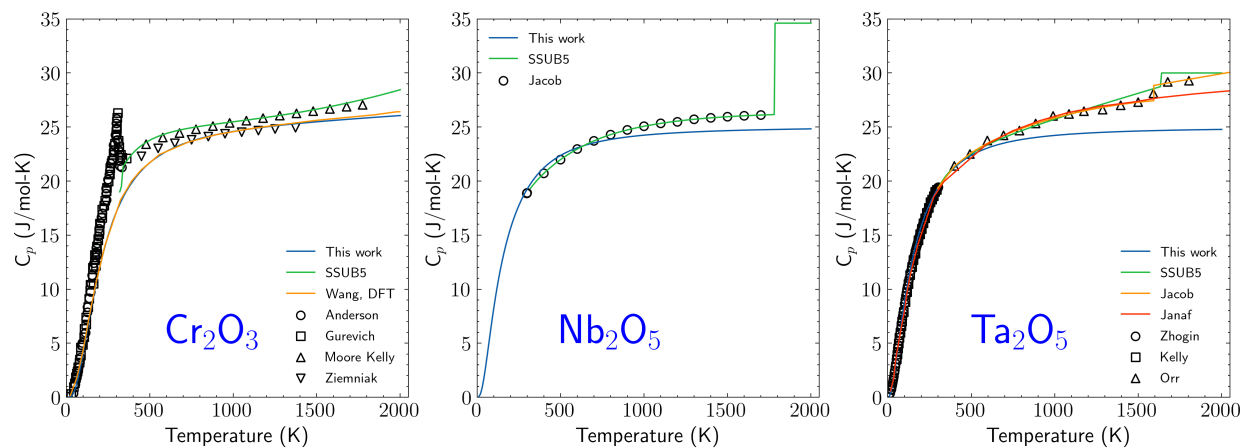


Figure 4. Heat capacity prediction of  $Cr_2O_3$ ,  $Nb_2O_5$  and  $Ta_2O_5$ , comparison with SSUB5 database and experimental data.

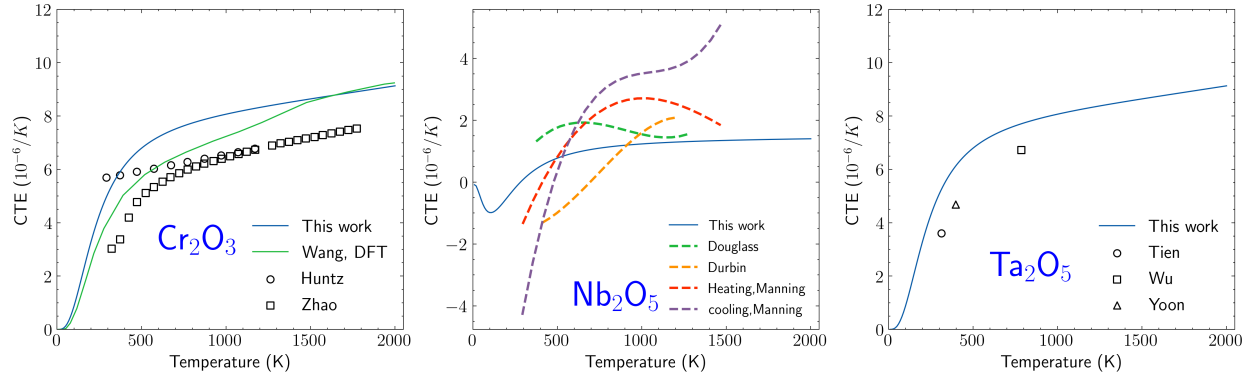


Figure 5. Linear thermal expansion of Cr<sub>2</sub>O<sub>3</sub>, Nb<sub>2</sub>O<sub>5</sub> and Ta<sub>2</sub>O<sub>5</sub>, comparison with the experimental data.

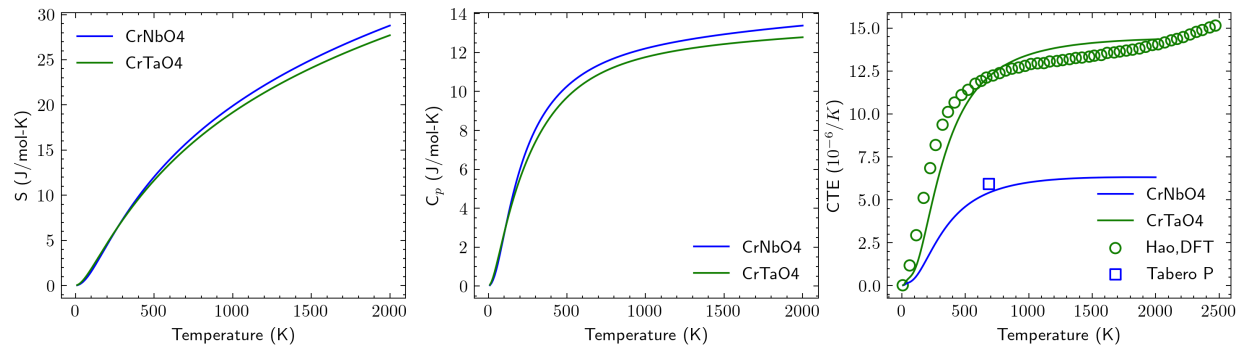


Figure 6. Thermodynamic properties, i.e., Entropy ( $S$ ), heat capacity ( $C_p$ ) and linear thermal expansion coefficient (CTE), prediction of  $\text{CrNbO}_4$  and  $\text{CrTaO}_4$  by this work.

## 7. Tables

Table 1. Setting details for DFT calculations

Oxides	$E_{\text{cut}}$ (eV)	k-Mesh electron	Supercell atoms phonon	k-Mesh phonon
$\text{Cr}_2\text{O}_3$	350	$8 \times 8 \times 8$	80	$4 \times 4 \times 4$
$\text{Nb}_2\text{O}_5$	350	$2 \times 8 \times 8$	56	$2 \times 4 \times 4$
$\text{Ta}_2\text{O}_5$	350	$8 \times 8 \times 2$	56	$4 \times 4 \times 2$
$\text{CrNbO}_4$	350	$6 \times 6 \times 7$	24	$6 \times 6 \times 7$
$\text{CrTaO}_4$	350	$6 \times 6 \times 7$	24	$6 \times 6 \times 7$

Table 2. Lattice information of Cr<sub>2</sub>O<sub>3</sub>, Nb<sub>2</sub>O<sub>5</sub>, Ta<sub>2</sub>O<sub>5</sub>, CrNbO<sub>4</sub> and CrTaO<sub>4</sub> in this work.

Oxides	Crystal system	Space group	a	b	c	$\alpha$	$\beta$	$\gamma$
Cr <sub>2</sub> O <sub>3</sub>	rhombohedral	R $\bar{3}c$	5.34 Å	5.34 Å	5.34 Å	55.15°	55.15°	55.15°
Nb <sub>2</sub> O <sub>5</sub>	Monoclinic	C12/m1	13.01 Å	3.86 Å	4.02 Å	90°	90.84°	90°
Ta <sub>2</sub> O <sub>5</sub>	Orthorhombic	Pmmn	3.82 Å	3.89 Å	12.97 Å	90°	90°	90°
CrNbO <sub>4</sub>	Tetragonal	I4 <sub>1</sub> md	6.62 Å	6.62 Å	6.05 Å	90°	90°	90°
CrTaO <sub>4</sub>	Tetragonal	I4 <sub>1</sub> md	6.59 Å	6.59 Å	6.03 Å	90°	90°	90°

Table 3. Equilibrium volume  $V_0$  and energy  $E_0$  of in CrNbO4 and CrTaO4 with different Cr spin configurations.

		Cr1	Cr2	Cr3	Cr4	$V_0(\text{\AA}^3)$	$E_0(\text{eV})$
CrNbO4	Str1	↑	↑	↑	↑	259.432	-196.872
	Str2	↑	↓	↑	↑	259.42	-196.871
	Str3	↓	↓	↑	↑	259.424	-196.871
	Str4	↑	↓	↑	↓	259.436	-196.871
CrTaO4	Str1	↑	↑	↑	↑	264.883	-205.837
	Str2	↓	↑	↑	↑	266.922	-205.773
	Str3	↓	↓	↑	↑	265.726	-205.831
	Str4	↓	↑	↓	↑	265.232	-205.813



## 8. References

- [1] O.N. Senkov, D.B. Miracle, K.J. Chaput, J.P. Couzinie, Development and exploration of refractory high entropy alloys - A review, *J Mater Res* 33 (2018) 3092–3128. <https://doi.org/10.1557/jmr.2018.153>.
- [2] B. Gorr, S. Schellert, F. Müller, H.-J. Christ, A. Kauffmann, M. Heilmaier, Current Status of Research on the Oxidation Behavior of Refractory High Entropy Alloys, *Adv Eng Mater* 23 (2021) 2001047. <https://doi.org/10.1002/adem.202001047>.
- [3] F. Müller, B. Gorr, H.-J. Christ, H. Chen, A. Kauffmann, M. Heilmaier, Effect of microalloying with silicon on high temperature oxidation resistance of novel refractory high-entropy alloy Ta-Mo-Cr-Ti-Al, *Materials at High Temperatures* 35 (2018) 168–176. <https://doi.org/10.1080/09603409.2017.1389115>.
- [4] B. Gorr, F. Müller, M. Azim, H.-J. Christ, T. Müller, H. Chen, A. Kauffmann, M. Heilmaier, High-Temperature Oxidation Behavior of Refractory High-Entropy Alloys: Effect of Alloy Composition, *Oxidation of Metals* 88 (2017) 339–349. <https://doi.org/10.1007/s11085-016-9696-y>.
- [5] S. Hao, Q.J. Hong, M.C. Gao, A prediction of the thermodynamic, thermophysical, and mechanical properties of CrTaO<sub>4</sub> from first principles, *Journal of the American Ceramic Society* 106 (2023) 7654–7669. <https://doi.org/10.1111/jace.19390>.
- [6] N. Esparza, V. Rangel, A. Gutierrez, B. Arellano, S.K. Varma, A comparison of the effect of Cr and Al additions on the oxidation behaviour of alloys from the Nb–Cr–Si system, *Materials at High Temperatures* 33 (2016) 105–114. <https://doi.org/10.1179/1878641315Y.0000000012>.
- [7] K.S. Chan, Cyclic oxidation response of multiphase niobium-based alloys, *Metallurgical and Materials Transactions A* 35 (2004) 589–597. <https://doi.org/10.1007/s11661-004-0370-7>.
- [8] S.Y. Qu, Y.F. Han, J.X. Song, Y.W. Kang, Effects of Cr and Al on High Temperature Oxidation Resistance of Nb-Si System Intermetallics, *Materials Science Forum* 546–549 (2007) 1485–1488. <https://doi.org/10.4028/www.scientific.net/MSF.546-549.1485>.
- [9] F. Müller, B. Gorr, H.J. Christ, J. Müller, B. Butz, H. Chen, A. Kauffmann, M. Heilmaier, On the oxidation mechanism of refractory high entropy alloys, *Corros Sci* 159 (2019). <https://doi.org/10.1016/j.corsci.2019.108161>.
- [10] Y. Wang, Z.-K. Liu, L.-Q. Chen, Thermodynamic properties of Al, Ni, NiAl, and Ni<sub>3</sub>Al from first-principles calculations, *Acta Mater* 52 (2004) 2665–2671. <https://doi.org/10.1016/j.actamat.2004.02.014>.
- [11] S.-L. Shang, Y. Wang, D. Kim, Z.-K. Liu, First-principles thermodynamics from phonon and Debye model: Application to Ni and Ni<sub>3</sub>Al, *Comput Mater Sci* 47 (2010) 1040–1048. <https://doi.org/10.1016/j.commatsci.2009.12.006>.

- [12] S. Shang, Y. Wang, Z.-K. Liu, First-principles calculations of phonon and thermodynamic properties in the boron-alkaline earth metal binary systems: B-Ca, B-Sr, and B-Ba, *Phys Rev B* 75 (2007) 024302. <https://doi.org/10.1103/PhysRevB.75.024302>.
- [13] G. Kresse, J. Furthmüller, Efficient iterative schemes for ab initio total-energy calculations using a plane-wave basis set, *Phys Rev B* 54 (1996) 11169–11186. <https://doi.org/10.1103/PhysRevB.54.11169>.
- [14] G. Kresse, D. Joubert, From ultrasoft pseudopotentials to the projector augmented-wave method, *Phys Rev B* 59 (1999) 1758–1775. <https://doi.org/10.1103/PhysRevB.59.1758>.
- [15] J.P. Perdew, K. Burke, M. Ernzerhof, Generalized Gradient Approximation Made Simple, *Phys Rev Lett* 77 (1996) 3865–3868. <https://doi.org/10.1103/PhysRevLett.77.3865>.
- [16] M. Methfessel, A.T. Paxton, High-precision sampling for Brillouin-zone integration in metals, *Phys Rev B* 40 (1989) 3616–3621. <https://doi.org/10.1103/PhysRevB.40.3616>.
- [17] A.I. Liechtenstein, V.I. Anisimov, J. Zaanen, Density-functional theory and strong interactions: Orbital ordering in Mott-Hubbard insulators, *Phys Rev B* 52 (1995) R5467–R5470. <https://doi.org/10.1103/PhysRevB.52.R5467>.
- [18] A. van de Walle, G. Ceder, The effect of lattice vibrations on substitutional alloy thermodynamics, *Rev Mod Phys* 74 (2002) 11–45. <https://doi.org/10.1103/RevModPhys.74.11>.
- [19] Y. Wang, L.-Q. Chen, Z.-K. Liu, YPHON: A package for calculating phonons of polar materials, *Comput Phys Commun* 185 (2014) 2950–2968. <https://doi.org/10.1016/j.cpc.2014.06.023>.
- [20] H. Schober, T. May, B. Dorner, D. Strauch, U. Steigenberger, Y. Morrii, Lattice dynamics of Cr<sub>2</sub>O<sub>3</sub>, *Zeitschrift für Physik B Condensed Matter* 98 (1995) 197–205. <https://doi.org/10.1007/BF01324525>.
- [21] A. Jain, S.P. Ong, G. Hautier, W. Chen, W.D. Richards, S. Dacek, S. Cholia, D. Gunter, D. Skinner, G. Ceder, K.A. Persson, Commentary: The Materials Project: A materials genome approach to accelerating materials innovation, *APL Mater* 1 (2013). <https://doi.org/10.1063/1.4812323>.
- [22] L. Androš Dubraja, D. Pajić, M. Vrankić, J. Dragović, M. Valant, M. Benčina, M. Jurić, Single-step preparation of rutile-type CrNbO<sub>4</sub> and CrTaO<sub>4</sub> oxides from oxalate precursors—characterization and properties, *Journal of the American Ceramic Society* 102 (2019) 6697–6704. <https://doi.org/10.1111/jace.16521>.
- [23] A. van de Walle, Multicomponent multisublattice alloys, nonconfigurational entropy and other additions to the Alloy Theoretic Automated Toolkit, *CALPHAD* 33 (2009) 266–278. <https://doi.org/10.1016/j.calphad.2008.12.005>.
- [24] Thermo-Calc Software and Databases, (2016).

- [25] J.O. Andersson, T. Helander, L. Höglund, P. Shi, B. Sundman, Thermo-Calc & DICTRA, computational tools for materials science, *CALPHAD* 26 (2002) 273–312. [https://doi.org/10.1016/S0364-5916\(02\)00037-8](https://doi.org/10.1016/S0364-5916(02)00037-8).
- [26] S. Klemme, H.St.C. O’Neill, W. Schnelle, E. Gmelin, The heat capacity of  $\text{MgCr}_2\text{O}_4$ ,  $\text{FeCr}_2\text{O}_4$ , and  $\text{Cr}_2\text{O}_3$  at low temperatures and derived thermodynamic properties, *American Mineralogist* 85 (2000) 1686–1693. <https://doi.org/10.2138/am-2000-11-1212>.
- [27] C.T. Anderson, The Heat Capacities of Chromium, Chromic Oxide, Chromous Chloride and Chromic Chloride at Low Temperatures <sup>1</sup>, *J Am Chem Soc* 59 (1937) 488–491. <https://doi.org/10.1021/ja01282a019>.
- [28] V.M. Gurevich, O.L. Kuskov, N.N. Smirnova, K.S. Gavrichev, A. V. Markin, Thermodynamic functions of eskolaite  $\text{Cr}_2\text{O}_3(\text{c})$  at 0–1800 K, *Geochemistry International* 47 (2009) 1170–1179. <https://doi.org/10.1134/S0016702909120027>.
- [29] Z.K. Liu, Y. Wang, S.-L. Shang, Zentropy Theory for Positive and Negative Thermal Expansion, *J Phase Equilibria Diffus* 43 (2022) 598–605. <https://doi.org/10.1007/s11669-022-00942-z>.
- [30] Z.K. Liu, N.L.E. Hew, S.-L. Shang, Zentropy theory for accurate prediction of free energy, volume, and thermal expansion without fitting parameters, *Microstructures* 4 (2024) 2024009. <https://doi.org/10.20517/microstructures.2023.56>.
- [31] Z.K. Liu, Thermodynamics and its prediction and CALPHAD modeling: Review, state of the art, and perspectives, *Calphad* 82 (2023) 102580. <https://doi.org/10.1016/j.calphad.2023.102580>.
- [32] Z.K. Liu, Quantitative Predictive Theories through Integrating Quantum, Statistical, and Equilibrium, and Nonequilibrium Thermodynamics, *Journal of Physics Condensed Matter Invited* (2024) ArXiv 2402.04143. <https://arxiv.org/abs/2402.04143>.
- [33] G.E. Moore, K.K. Kelly, U.S. Bureau of Mines Technical Report, 662 (1944).
- [34] Y. Wang, H. Fang, C.L. Zacherl, Z. Mei, S. Shang, L.Q. Chen, P.D. Jablonski, Z.K. Liu, First-principles lattice dynamics, thermodynamics, and elasticity of  $\text{Cr}_2\text{O}_3$ , *Surf Sci* 606 (2012) 1422–1425. <https://doi.org/10.1016/j.susc.2012.05.006>.
- [35] S.E. Ziemniak, L.M. Anovitz, R.A. Castelli, W.D. Porter, Thermodynamics of  $\text{Cr}_2\text{O}_3$ ,  $\text{FeCr}_2\text{O}_4$ ,  $\text{ZnCr}_2\text{O}_4$ , and  $\text{CoCr}_2\text{O}_4$ , *J Chem Thermodyn* 39 (2007) 1474–1492. <https://doi.org/10.1016/j.jct.2007.03.001>.
- [36] A.M. Huntz, A. Piant, J.L. Lebrun, S. Daghigh, Evidence of stress relaxation in thermally grown oxide layers—experiments and modelling, *Materials Science and Engineering: A* 248 (1998) 44–55. [https://doi.org/10.1016/S0921-5093\(98\)00519-X](https://doi.org/10.1016/S0921-5093(98)00519-X).
- [37] P. Zhao, H. Zhao, J. Yu, H. Zhang, H. Gao, Q. Chen, Crystal structure and properties of  $\text{Al}_2\text{O}_3\text{-Cr}_2\text{O}_3$  solid solutions with different  $\text{Cr}_2\text{O}_3$  contents, *Ceram Int* 44 (2018) 1356–1361. <https://doi.org/10.1016/j.ceramint.2017.08.195>.

- [38] M. Arrigoni, G.K.H. Madsen, Comparing the performance of LDA and GGA functionals in predicting the lattice thermal conductivity of III-V semiconductor materials in the zincblende structure: The cases of AlAs and BAs, *Comput Mater Sci* 156 (2019) 354–360. <https://doi.org/10.1016/j.commatsci.2018.10.005>.
- [39] J. Mougín, A. Galerie, M. Dupeux, N. Rosman, G. Lucazeau, A.-M. Huntz, L. Antoni, In-situ determination of growth and thermal stresses in chromia scales formed on a ferritic stainless steel, *Materials and Corrosion* 53 (2002) 486–490. [https://doi.org/10.1002/1521-4176\(200207\)53:7<486::AID-MACO486>3.0.CO;2-P](https://doi.org/10.1002/1521-4176(200207)53:7<486::AID-MACO486>3.0.CO;2-P).
- [40] K.T. Jacob, C. Shekhar, M. Vinay, Y. Waseda, Thermodynamic Properties of Niobium Oxides, *J Chem Eng Data* 55 (2010) 4854–4863. <https://doi.org/10.1021/je1004609>.
- [41] M. Chase Jr, JANAF thermochemical tables third edition, *J. Phys. Chem. Ref. Data* 14 (1985).
- [42] Z.-K. Liu, N.L.E. Hew, S.-L. Shang, Zentropy theory for accurate prediction of free energy, volume, and thermal expansion without fitting parameters, *Microstructures* 4 (2024). <https://doi.org/10.20517/microstructures.2023.56>.
- [43] W.R. MANNING, O. HUNTER, F.W. CALDERWOOD, D.W. STACY, Thermal Expansion of Nb<sub>2</sub>O<sub>5</sub>, *Journal of the American Ceramic Society* 55 (1972) 342–347. <https://doi.org/10.1111/j.1151-2916.1972.tb11306.x>.
- [44] E. A. Durbin, C. G. Harman, Tech. Rept, Tech. Rept BMI-792 (1952).
- [45] D.L. Douglass, The thermal expansion of niobium pentoxide and its effect on the spalling of niobium oxidation films, *Journal of the Less Common Metals* 5 (1963) 151–157. [https://doi.org/10.1016/0022-5088\(63\)90008-0](https://doi.org/10.1016/0022-5088(63)90008-0).
- [46] H. Choosuwan, R. Guo, A.S. Bhalla, U. Balachandran, Negative thermal expansion behavior in single crystal and ceramic of Nb<sub>2</sub>O<sub>5</sub>-based compositions, *J Appl Phys* 91 (2002) 5051–5054. <https://doi.org/10.1063/1.1464232>.
- [47] F. Holtzberg, A. Reisman, M. Berry, M. Berkenblit, Chemistry of the Group VB Pentoxides. VI. The Polymorphism of Nb<sub>2</sub>O<sub>5</sub>, *J Am Chem Soc* 79 (1957) 2039–2043. <https://doi.org/10.1021/ja01566a004>.
- [48] B.M. Gatehouse, A.D. Wadsley, The crystal structure of the high temperature form of niobium pentoxide, *Acta Crystallogr* 17 (1964) 1545–1554. <https://doi.org/10.1107/S0365110X6400384X>.
- [49] G. Brauer, Die Oxyde des Niobs, *Z Anorg Allg Chem* 248 (1941) 1–31. <https://doi.org/10.1002/zaac.19412480101>.
- [50] H. Schäfer, G. Breil, Über Das System Nb<sub>2</sub>O<sub>5</sub>—Ta<sub>2</sub>O<sub>5</sub>—NbO<sub>2</sub>—TaO<sub>2</sub>—H<sub>2</sub>O—H<sub>2</sub>, *Z Anorg Allg Chem* 267 (1952) 265–276. <https://doi.org/10.1002/zaac.19522670410>.

- [51] K.T. Jacob, C. Shekhar, Y. Waseda, An update on the thermodynamics of Ta<sub>2</sub>O<sub>5</sub>, *J Chem Thermodyn* 41 (2009) 748–753. <https://doi.org/10.1016/j.jct.2008.12.006>.
- [52] R.L. Orr, High-temperature Heat Contents of Tantalum and Niobium Oxides, *J Am Chem Soc* 75 (1953) 2808–2809. <https://doi.org/10.1021/ja01108a005>.
- [53] S.G. Yoon, Y.T. Kim, H.K. Kim, M.J. Kim, H.M. Lee, D.H. Yoon, Comparison of residual stress and optical properties in Ta<sub>2</sub>O<sub>5</sub> thin films deposited by single and dual ion beam sputtering, *Materials Science and Engineering: B* 118 (2005) 234–237. <https://doi.org/10.1016/j.mseb.2004.12.055>.
- [54] S. Wu, H.M. Chan, M.P. Harmer, Compositional tailoring of the thermal expansion coefficient of tantalum (V) oxide, *J Mater Sci* 41 (2006) 689–695. <https://doi.org/10.1007/s10853-006-6487-x>.
- [55] C.L. Tien, C.C. Lee, K.P. Chuang, C.C. Jaing, Simultaneous determination of the thermal expansion coefficient and the elastic modulus of Ta<sub>2</sub>O<sub>5</sub> thin film using phase shifting interferometry, *J Mod Opt* 47 (2000) 1681–1691. <https://doi.org/10.1080/09500340008231417>.
- [56] P. Tabero, Thermal expansion of MNbO<sub>4</sub> phases where M=Al, Cr, Fe, Ga, *J Therm Anal Calorim* 88 (2007) 269–272. <https://doi.org/10.1007/s10973-006-8049-5>.